Journal of Materials Chemistry

Cite this: J. Mater. Chem., 2012, 22, 17893

www.rsc.org/materials

PAPER

A hybrid ink of binary copper sulfide nanoparticles and indium precursor solution for a dense $CuInSe_2$ absorber thin film and its photovoltaic performance†

Ara Cho,[ab] SeJin Ahn,[b] Jae Ho Yun,[b] Jihye Gwak,[b] Hyunjoon Song*[a] and Kyunghoon Yoon*[b]

Received 26th April 2012, Accepted 4th July 2012
DOI: 10.1039/c2jm32624h

A newly developed hybrid ink of binary CuS nanoparticles and In precursor solution was prepared to form a $CuInSe_2$ (CIS) thin film. Previously, we have shown a CIS thin film solar cell with 4.19% conversion efficiency using the hybrid ink of $Cu_{2-x}Se$ nanoparticles and In precursor. Deposition using hybrid ink offers advantages including the provision of stress-relief and crack-deflection centers by pure material based nanoparticles and effective binding with the nanoparticles by precursor solutions without other organic binders. Here, we demonstrate volume expansion of a thin film for forming a well-grown absorber layer using CuS nanoparticles instead of $Cu_{2-x}Se$. Binary nanoparticles were synthesized by a low temperature colloidal process and a precursor solution was prepared by using a non-toxic chelating agent to disperse the In component stably. The band gap of the CIS thin film was 1.08 eV, as determined by external quantum efficiency (EQE) measurements, and the reproducible conversion efficiency of the fabricated device was 6.23%.

1. Introduction

Interest in renewable energy using natural resources is rising tremendously in the face of recent environmental challenges. Among other natural resources, solar energy using energy- and cost-efficient photovoltaic cells has been spotlighted as a solution to major environmental problems. In particular, $Cu(In,Ga)Se_2$ (CIGS) has been studied widely as a light absorber in photovoltaic cells due to its high light absorption coefficient ($\sim 10^5$ cm^{-1}) and tunable direct band gap (1.0–2.4 eV) *via* control over the In/Ga and S/Se ratios. Owing to these characteristics, many researchers are interested in manufacturing CIGS solar cells because thin layers (1–2 μm) can be used as an absorber in the CIGS solar cells, in contrast to the well-known 100–300 μm thick crystalline Si solar cells on the market.

Although up to 20% conversion efficiency of CIGS solar cells has been reported recently,[1] high production costs and material waste during processing remain significant obstacles to replace traditional vacuum-based processes such as multi-stage co-evaporation and sputtering + selenization.[2] On the other hand, non-vacuum processes are cost-effective and there is less material waste, because there is no need for expensive vacuum equipment, enormous energy, or excess materials to deposit CIGS thin films.[2–15] Therefore, many researchers have recently investigated non-vacuum coating processes as complementary deposition techniques for fabricating CIGS thin film solar cells. Furthermore, an efficiency of 17.1%, the highest value documented to date, was reported for a non-vacuum processed CIGS solar cell from Nanosolar and certified by the National Renewable Energy Laboratory (NREL).[16]

However, despite the cost-effectiveness and ease of operation in non-vacuum processes, some challenges must still be addressed. Non-vacuum processes are typically split into two categories, particle-based and solution-based. In particle-based processes,[3–8] it is relatively easy to remove excess organics from solvents through the pores between particles. In addition, the particles can be synthesized with high purity, but the process is complicated. On the other hand, in the case of solution-based processes,[9–15] it is easy to make precursor solutions but difficult to remove excess organics from solvents and precursors, especially carbon.[13]

To overcome these challenges, deposition using hybrid ink provides a possible means of encompassing beneficial characteristics of particle-based and solution-based processes to achieve low-cost and high-efficiency CIGS thin film solar cells. In the hybrid ink, both particles and precursor solutions are incorporated, allowing the formation of dense thin films. Particles composed of pure materials in the hybrid ink act as supporters of the layer structure within precursor solutions and stress-relief/crack-deflection centers in the deposition of layers compared to layers using only solution processes. Precursor solutions in the

[a]*Department of Chemistry, Korea Advanced Institute of Science and Technology, Daejeon, Republic of Korea 305-701. E-mail: hsong@kaist.ac.kr*
[b]*Photovoltaic Center, Korea Institute of Energy Research, 102 Gajeong-ro, Yuseong-gu, Daejeon, Republic of Korea 305-343. E-mail: y-kh@kier.re.kr*
† Electronic supplementary information (ESI) available. See DOI: 10.1039/c2jm32624h

hybrid ink have dissolved components that can make compact layers through effective binding with the nanoparticles, and act as organic binders, thus removing the need for other organic binders. Mitzi *et al.* reported a hybrid solution–particle approach for an earth-abundant $Cu_2ZnSn(S,Se)_4$ (CZTS) system.[14] However, toxic hydrazine was used as a solvent for dissolving metal chalcogenides to fabricate a CZTS absorber layer in connection with CIGS absorber layers using a solution-based toxic hydrazine method in their earlier work.[9,10]

In our previous work, a non-vacuum processed CIS thin film solar cell using the hybrid ink method was proposed, focusing on a non-toxic and chelating precursor solution in the hybrid ink with binary $Cu_{2-x}Se$ nanoparticles as a proof-of-concept.[17] However, even though up to 4% conversion efficiency was obtained, some voids and insufficiently grown grains were found. Hillhouse *et al.* reported the use of $Cu(In,Ga)S_2$ nanocrystals instead of $CuInSe_2$ nanocrystals to reduce voids and grow CIGS grains.[3,5] The replacement of S in $Cu(In,Ga)S_2$ nanocrystals by Se during selenization caused volume expansion of the film, and larger grains were consequently obtained in the CIGS thin film.

In this work, we exploit the characteristics of volume expansion using CuS nanoparticles instead of $Cu_{2-x}Se$ nanoparticles to prepare the hybrid ink. Binary CuS nanoparticles were synthesized by a low temperature colloidal process and an In precursor solution was arranged as a chelating agent and a binder. During the process, S in CuS was replaced by Se vapor and a dense CIS thin film was then formed *via* volume expansion due to the replacement of S with Se. As a result, a CIS thin film using a hybrid ink of CuS nanoparticles and In precursor has larger grains and approximately 2% greater efficiency than that of our previous work.

2. Experimental section

2.1. Reagents

Copper(I) iodide, CuI (99.998%, Alfa Aesar), sodium sulfide, Na_2S (99.8%, Alfa Aesar), methanol, CH_3OH (MeOH, 99.6%, Junsei), pyridine, C_5H_5N (anhydrous, 99.8%, Aldrich), indium(III) acetate, $In(CH_3COO)_3$ ($In(Ac)_3$, 99.99%, Aldrich), and monoethanolamine, $NH_2CH_2CH_2OH$ (MEA, 99.0%, Aldrich) are the analytical reagents. The elemental Se (99.999%, 3 mm shot) was purchased from Cerac. All chemicals were used as received without further purification and stored in a nitrogen filled glove box to prevent air or humidity from inducing degradation. The Mo-coated soda lime glass was fabricated using a lab-made DC sputtering system with a thickness of approximately 1 μm.

2.2. Synthesis of colloidal CuS nanoparticles

The typical synthetic method for fabricating colloidal CuS nanoparticles was performed according to the colloidal synthetic process as follows:[6] in a nitrogen filled glove box, CuI (2 mmol) and Na_2S (1 mmol) were dissolved in 30 ml of pyridine and 20 ml of methanol, respectively, and stirred for 10 min. The thoroughly dissolved CuI (yellowish) and Na_2S (clear) solutions were taken from the glove box and mixed together in a 100 ml glass bottle under a fume hood. The mixed solution in the bottle was stirred continuously in an ice-bath at a set temperature of 0 °C for 7 min; a black colloidal solution was obtained. The colloidal solution was then centrifuged at 10 000 rpm for 10 min, the upper layer liquid was decanted, and the isolated colloids were dispersed in methanol. The above centrifugation and isolation procedure was repeated several times for purification. Finally, the CuS colloidal nanoparticles were redispersed in methanol or dried in air for measurement.

2.3. Preparation of hybrid ink

The hybrid ink was prepared with $In(Ac)_3$, MeOH, and MEA as a chelating agent and a binder. $In(Ac)_3$ was mixed with MEA and MeOH in a 10 ml vial and dissolved thoroughly by ultra-sonication. Synthesized CuS particles were added to the $In(Ac)_3$ dissolved solution and sonicated for 3 hours. In this case, the CuS : $In(Ac)_3$ molar ratio was approximately 5 : 1 due to control of the Cu/In ratio and the $In(Ac)_3$: MEA molar ratio was 1 : 6 due to adequate coordination between MEA and In. The CuS : MeOH (in $In(Ac)_3$ dissolved solution) ratio was 1 : 4 by weight; however, in order to adjust the viscosity of the precursor ink for the spin-coating step, the quantity of MeOH was controlled by using the individual coating procedure. All preparation processes were performed at room temperature in ambient air.

2.4. Thin film deposition and selenization

Precursor films were deposited on a 1 μm thick Mo-coated soda lime glass using a spin coater (ACE-200, Dong Ah Tech., Korea) under conditions of 2000 rpm and 20 s. The samples were then dried at 80 °C, 120 °C, and 200 °C for 5 min in air on a hot plate to evaporate the MeOH and MEA. This process was repeated three times. The selenization was performed in a vacuum evaporator equipped with a Knudsen-type effusion cell. The chamber was initially evacuated to a base pressure of 5×10^{-6} torr with a turbo molecular pump and then the elemental Se was evaporated from the effusion cell. The typical substrate temperature and selenization time were 530 °C and 60 min, respectively (Fig. 1). During the selenization in Fig. 1, the Se vapor was supplied by opening a shutter to the substrate at a substrate temperature of 200 °C in order to maintain a sufficient Se atmosphere. After the reaction, the Se vapor was supplied until the substrate

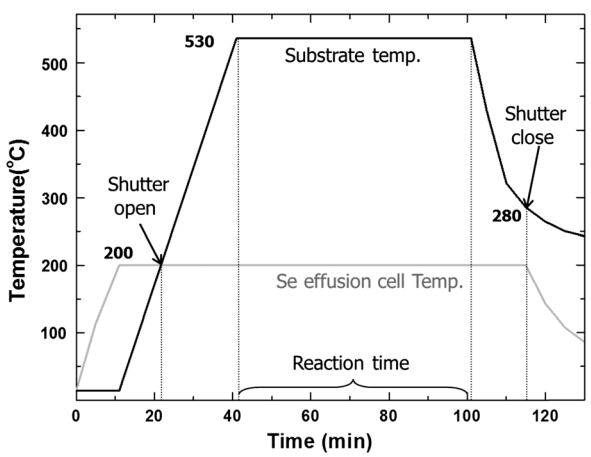

Fig. 1 A typical temperature profile of selenization.

temperature reached approximately 280 °C in order to prevent the deposition of Se as well as to maintain sufficient Se in the atmosphere. The flux of the Se vapor was regulated by the effusion cell temperature and was indicated as the deposition rate with the unit of Å s^{-1} using a quartz crystal microbalance (QCM).

2.5. Solar cell fabrication

Solar cells were fabricated according to the conventional Mo/CIS/CdS/i-ZnO/n-ZnO/Al structure. A 60 nm thick CdS buffer layer was deposited on a CIS film by a chemical bath deposition (CBD) method and i-ZnO (50 nm)/Al-doped n-ZnO (500 nm) was deposited by radio-frequency (rf) magnetron sputtering on the CdS layer. An Al grid of 500 nm thickness was deposited as a current collector using thermal evaporation. The active area of completed cells was 0.4848 cm^2.

2.6. Characterization and analysis

The morphologies and compositions of the particles, as-deposited films, and selenized films were analyzed using high resolution scanning electron microscopy (HRSEM, XL30SFEG Phillips Co., Holland at 10 kV) and energy dispersive spectroscopy (EDS, EDAX Genesis apex, acceleration voltage: 30 kV, collection time: 100 s with the standard-less method), respectively. An elemental analysis of the solution in the hybrid ink was carried out using inductively coupled plasma (ICP, PolyScan 61 E mono, Thermo Jarrel Ash). The crystalline structure of the films was identified using X-ray diffraction (XRD, Rigaku Japan, D/MAX-2500) with a CuKα line and Raman spectroscopy. The Raman spectra were taken in a quasi-backscattering geometry using the 514.5 nm line of an Ar ion laser as the excitation source. The scattered light was filtered with a holographic edge filter, dispersed using a TRIAX 320 spectrometer, and detected with a liquid-nitrogen-cooled, back-illuminated charge-coupled-device (CCD) detector array. The depth compositional profile of the selenized film was obtained by Auger electron spectroscopy (AES, Perkin Elmer, SAM 4300).

Device performances including the conversion efficiency and the EQE (External Quantum Efficiency) were characterized using a class AAA solar simulator (WXS-155S-L2, WACOM, Japan) and an IPCE (Incident Photon Conversion Efficiency) measurement unit (PV Measurements, Inc., USA), respectively. Also, the doping concentration was investigated by *C–V* (Capacitance–Voltage) analysis for the completed solar cells.

3. Results and discussion

3.1. Characterization of colloidal CuS nanoparticles

To prepare the hybrid ink in this work, binary CuS nanoparticles and an In precursor solution with $In(Ac)_3$ as a precursor, MEA as a binder, and MeOH as a dispersant were used. Binary CuS nanoparticles were synthesized *via* a low temperature colloidal process. Fig. 2(a) shows a typical SEM image of the CuS nanoparticles. The synthesized colloidal nanoparticles have various diameter sizes ranging from several nanometers to a few hundred nanometers, with an average diameter of 20 nm, which is smaller than those of $Cu_{2-x}Se$ nanoparticles (~50 nm) in a previous report.[17] However, even though the average size of CuS nanoparticles is smaller than that of $Cu_{2-x}Se$ nanoparticles, the synthesized colloidal nanoparticles agglomerated together and displayed diverse shapes from oval to round.

In Fig. 2(b), the XRD pattern was identified as a hexagonal CuS structure (Covellite, JCPDS# 06-0464, 3.792 Å × 3.792 Å × 16.344 Å) with major (102), (103), and (111) plane reflections. Even though the ratio of Cu/S during the nanoparticle synthesis was 2, a characteristic XRD pattern of a Cu_2S structure was not detected. This is attributed to the nanoparticle synthetic process being performed under ambient air, with the result that Cu^{2+} in CuS was produced from oxidation of Cu^+ into Cu^{2+} due to surface oxygen in the ambient air.[18,19]

3.2. Characterization of CIS thin films with the hybrid ink

The hybrid ink was prepared with the CuS characterized above and $In(Ac)_3$ dissolved in MEA and MeOH. When $In(Ac)_3$ was dissolved in MEA and MeOH, In-complexes were expected to form after the dissolving reaction. The indium (In) precursor solution was a pale-yellowish clear liquid; however, after mixing the In precursor solution with CuS nanoparticles, the solution turned deep blue. According to the ICP elemental analysis, 372 ppm of Cu was detected in the solution of the hybrid ink after precipitating CuS nanoparticles. From this result, it was inferred that blue colored Cu(II) in CuS diffused out by a chelating effect of the amine group in MEA and formed complexes.[20–22]

Fig. 3 shows the XRD patterns of as-deposited and selenized thin films obtained at 530 °C for 60 min with a Se deposition rate of 100 Å s^{-1}. The XRD pattern of the as-deposited thin film was amorphous due to the characteristics of the In precursor solution. On the other hand, the selenized film showed only clear CIS phases (JCPDS# 40-1487, tetragonal 5.782 Å × 5.782 Å × 11.619 Å) even though CuS was used as a particulate precursor. It is inferred that S in CuS was replaced by Se vapor during the selenization process. The EDS analysis showed that the Cu/In ratios of the as-deposited and selenized thin films were 0.53 and 0.64, respectively. The Cu/In ratios of selenized thin films are generally much larger than the ratios of as-deposited thin films. This phenomenon can be explained by the formation of volatile In_2Se during selenization and subsequent evaporation due to the high vapor pressure of In_2Se.[23–25] However, in the present work, the Cu/In ratio of the selenized thin film was similar to the ratio of the as-deposited thin film. It was assumed that the MEA in the hybrid ink held In in a complex form, such as the Cu–MEA complex described above, and thus the In in the hybrid ink is less likely to form volatile In_2Se by a chelating effect of MEA during the selenization process.

Fig. 4 shows planar and cross-sectional SEM images of (a) as-deposited and (b) selenized films at 530 °C for 60 min with a Se deposition rate of 100 Å s^{-1}. As seen in Fig. 4(a), no pores or cracks are formed in the as-deposited thin film during the drying procedure, and the layer is roughly 2.17 μm thick. After selenization (Fig. 4(b)), almost no pores were observed on the surface but a double-layered structure was observed in the cross-sectional image. The thicknesses of the upper layer and bottom layer were 1.04 μm and 1.46 μm, respectively. Selenized thin films are typically thinner than as-deposited thin films due to the removal of excess organics. However, in the present work, the

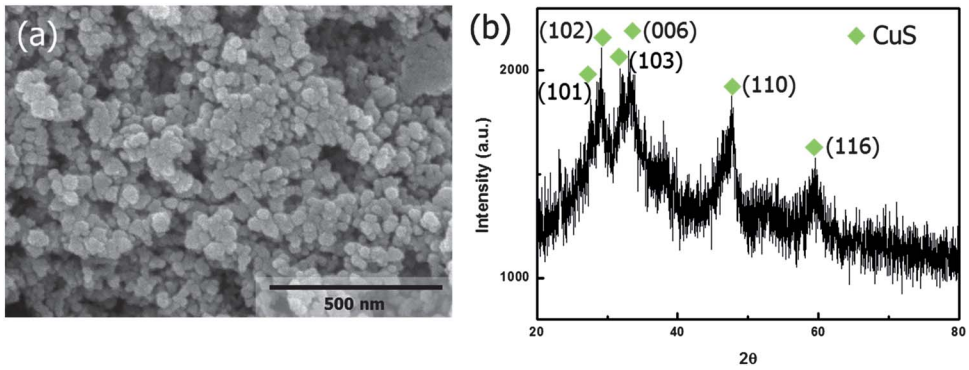

Fig. 2 (a) SEM image and (b) XRD pattern of the synthesized CuS nanoparticles.

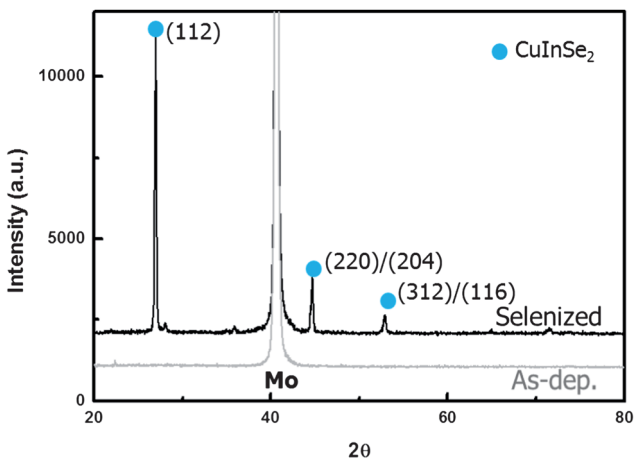

Fig. 3 XRD patterns of as-deposited and selenized thin films.

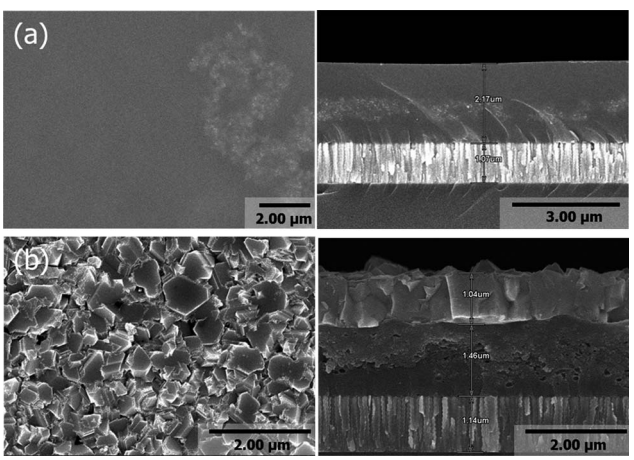

Fig. 4 Planar and cross-sectional SEM images of (a) as-deposited film and (b) selenized film.

thickness of the selenized thin film was slightly greater than that of the as-deposited thin film. It is assumed that the position of S in CuS was replaced by Se, which resulted in a dense CIS thin film *via* volume expansion during the process. As compared with the fabricated CIS thin film using a hybrid ink of $Cu_{2-x}Se$ nanoparticles and In precursor solution,[17] the grains were bigger and the upper CIS layer was also thicker in the selenized CIS thin film using a hybrid ink of CuS nanoparticles and In precursor solution.

Fig. 5 displays the Raman spectra of selenized thin films using $Cu_{2-x}Se$ nanoparticles (I) and CuS nanoparticles (II) in the hybrid ink. Normally, the dominant CIS A_1 vibrational mode is observed at around 173 cm^{-1} corresponding to the Se–Se vibration[26] and a S analogue of CIS is known to have A_1 vibrational mode at around 290 cm^{-1} corresponding to the S–S vibration.[27] In Fig. 5, both spectra had a dominant peak at around 173 cm^{-1}, which is a characteristic CIS A_1 vibrational mode;[26] however, spectrum I obtained using $Cu_{2-x}Se$ nanoparticles had an OVC ($CuIn_5Se_8$) peak whereas spectrum II derived using CuS nanoparticles had no other peaks, including even those related to S or CuS. It is inferred that almost all S in CuS was replaced by Se during the selenization and a CIS thin film was then formed. According to Scheer *et al.*,[28] the spectral features of the A_1 mode provide a direct indication of the crystalline quality of a material. Therefore, it is assumed that the sharp and intense A_1 mode in spectrum II using CuS nanoparticles compared to that of spectrum I using $Cu_{2-x}Se$ nanoparticles reveals that high quality CIS was formed *via* volume expansion due to the replacement of S by Se during the selenization.

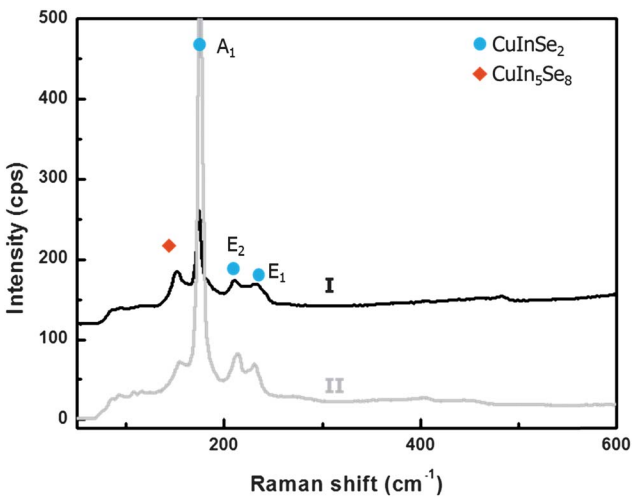

Fig. 5 Raman spectra of selenized thin films (I: CIS using $Cu_{2-x}Se$ nanoparticles and II: CIS using CuS nanoparticles in this work).

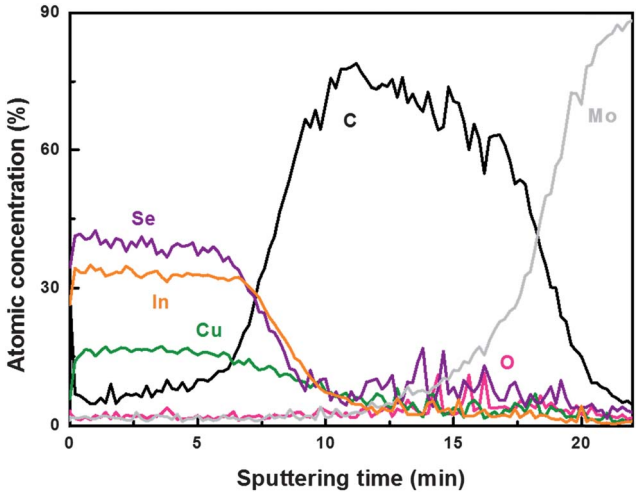

Fig. 6 AES depth profiles of selenized film.

For a compositional analysis of the double-layer, an AES depth profile was performed and the results are given in Fig. 6. From the AES depth profile, the upper layer was a CIS compound with a flat Cu/In ratio and the bottom layer was mainly composed of carbon. From the cross-sectional SEM image and the AES depth profile of the selenized film, it was assumed that, during the selenization, the CIS chalcopyrite phase formed starting from the surface by the In–MEA complex and the Cu–MEA complex in the precursor solution with the supply of Se vapor. The CIS formation reaction then proceeded with CuS nanoparticles, Se vapor, and the precursor solution to produce a dense CIS phase in the upper layer *via* volume expansion by the replacement of S with Se. At the same time, the densely formed CIS blocked the evaporation of residual carbons from the precursor solution.[13] However, according to the AES profile in Fig. 6, the residual In and Se from the In precursor solution and the Se vapor remained in the bottom layer. Thus, the bottom layer would function as a current flow path rather than as an insulating layer in a working device.

3.3. Device performances of fabricated CIS thin film solar cells

The double layered CIS/carbon thin film was tested as an absorber layer for a thin film solar cell device. The conventional CIGS solar cell has a SLG/Mo/CIGS (absorber layer)/CdS/i-ZnO/n-ZnO/Al structure. Light illuminated and dark current density–voltage (*J–V*) characteristics are presented in Fig. 7(a). The obtained device performance showed a power conversion efficiency (E_{ff}) of 6.23% with an open-circuit voltage (V_{OC}), short-circuit current density (J_{SC}), and fill factor (FF) of 0.42 V, 31.01 mA cm^{-2}, and 0.48, respectively. These values were higher than those of our previous work[17] ($E_{ff} = 4.19\%$); this is mostly attributed to the increase of J_{sc} due to the higher CIS crystalline quality *via* volume expansion from the replacement of S with Se during the selenization, which was confirmed by SEM images and the Raman spectra. However, the efficiency was still limited, particularly by a low FF, indicating that the cell has a high shunt conductance (G_{sh}) and a high series resistance (R_s). To extract the R_s of the cell, the light *J–V* curve was redrawn in a *R–J* form. In Fig. 7(b), the *R–J* curve of a CIS device with a conversion

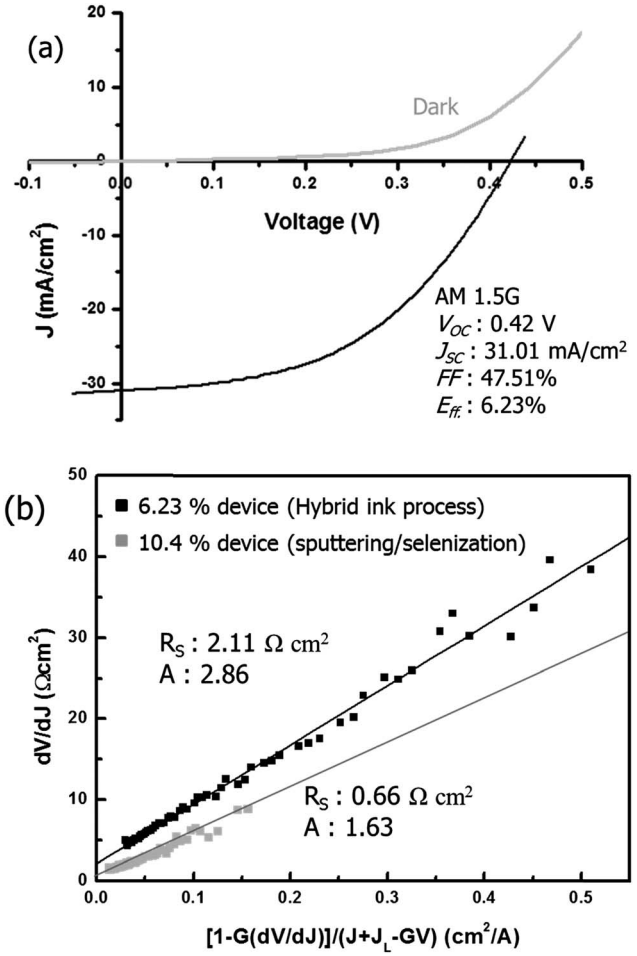

Fig. 7 (a) Light and dark *J–V* characteristics of the cell. Light illuminated *J–V* was measured by using a class AAA solar simulator (AM 1.5G, 100 mW cm^{-2}) at 25 °C. (b) *R–J* curves of CIS solar cells from a 6.23% efficiency device *via* the hybrid ink process and a 10.4% efficiency device *via* a sputtering/selenization process, for comparison.

efficiency of 10.4% fabricated by a sputtering and selenization process in our laboratory is also shown for comparison. The R_s value of the 6.23% efficiency device was found to be almost 3 times larger than that of the 10.4% efficiency device. The shunt conductance (*G*) of the 6.23% efficiency device was calculated to be 1.71 mS cm^{-2}. This value is higher than those of high efficiency CIGS solar cells (<1 mS cm^{-2}). The ideality factor (*A*) also showed that interface recombination by tunneling ($A > 2$) was dominant for the 6.23% efficiency device corresponding to the low FF. In the case of the low ideality factor of the 10.4% efficiency device ($1 < A < 2$), bulk recombination was dominant.[29] From these results, it was inferred that the 6.23% efficiency device suffered from high R_s, which was caused by the resistive carbon layer placed between the CIS and Mo layers even though the carbon layer was not electrically insulating in this case.

Fig. 8 shows (a) the EQE curve and (b) the band gap of the CIS layer determined from the long-wavelength region of the EQE curve. In the EQE curve (Fig. 8(a)), a long tail decreased gradually from 570 nm. This was attributed to the short minority carrier (electron) diffusion length and incomplete light absorption due to insufficient thickness of the absorber layer. The J_{SC}

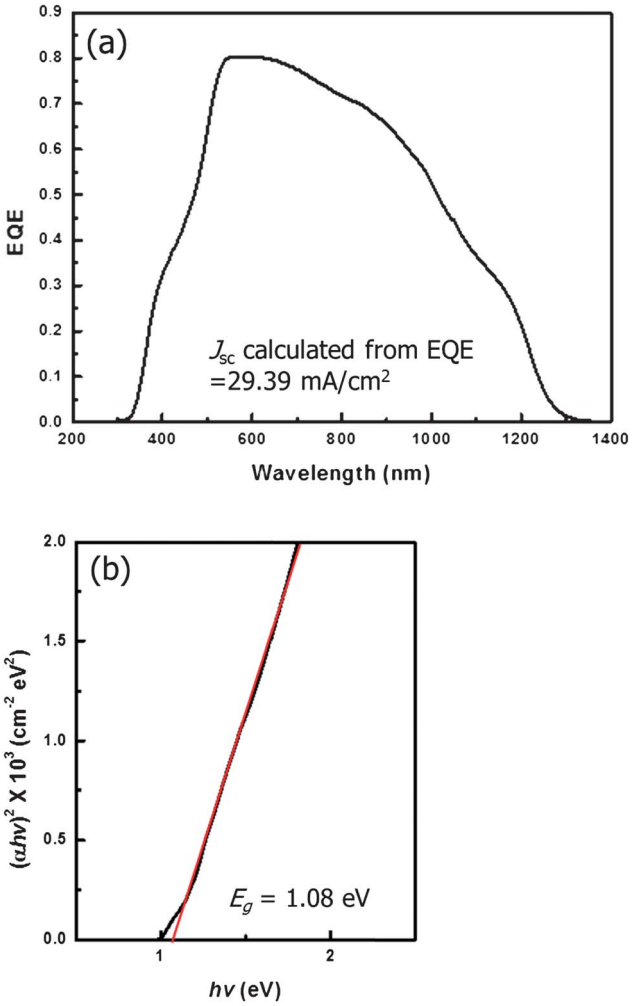

Fig. 8 (a) EQE curve and (b) determination of band gap from the $[h\nu \times \ln(1 - \mathrm{EQE})]^2$ *vs.* $h\nu$ relation.

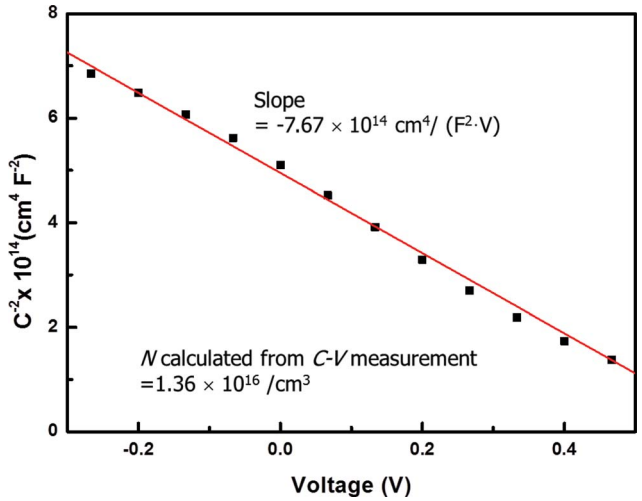

Fig. 9 $1/C^2$ *vs.* V curve of the fabricated CIS solar cell, measured at 100 kHz.

was also calculated from the spectral response of EQE data and the value (29.39 mA cm^{-2}) was similar to the measured value (in Fig. 7(a)) from the solar simulator. The band gap of the CIS layer was determined from the $[h\nu \times \ln(1 - \mathrm{EQE})]^2$ against $h\nu$ relation,[30] showing a value of 1.08 eV, which corresponds to the band gap of CIS (1.04 eV) in other studies.[31,32]

Fig. 9 shows the $(1/C^2)$–V curve providing data about the examination of the semiconductor properties and the carrier concentration. From the negative value of the slope, the fabricated CIS thin film was identified as a p-type semiconductor and the net carrier concentration was calculated by the following relation:[33]

$$N = (2/q\varepsilon A^2)\, \mathrm{d}V/\mathrm{d}(1/C^2),$$

where N is the net carrier concentration, ε is the permittivity, A is the area, C is the capacitance, and V is the applied voltage.

According to the NREL, the carrier concentration from CIGS devices with efficiencies greater than 19% was about 2×10^{16} cm^{-3}.[34] The calculated carrier concentration of the hybrid ink processed CIS solar cell was 1.36×10^{16} cm^{-3}, which is within the boundary of a typical value of a CIGS device. In spite of the typical value of the net carrier concentration, the CIS solar cell fabricated with hybrid ink showed lower conversion efficiency than that of vacuum-processed CIGS solar cells. It was assumed that the resistive carbon layer between the CIS and Mo layers impeded active current flow even though the net carrier concentration of the hybrid ink-processed CIS device was similar to that of vacuum-processed CIGS devices.

As reported above, in spite of still low conversion efficiency compared to that obtained with a typical vacuum process, the hybrid ink process using binary nanoparticles and a precursor solution with a chelating agent is an economical strategy to form an absorber layer. Notably, CuS nanoparticles were used to form a dense CIS layer *via* volume expansion due to the replacement of S with Se. For the next step to achieve improved performance, we will focus on the formation of a dense and thick CIS upper layer and reducing carbon in the bottom layer.

4. Conclusions

A hybrid ink process was introduced to form CIS thin films. The hybrid ink consisted of synthesized binary nanoparticles as stress-relief and crack-deflection centers and a precursor solution for effective binding with the nanoparticles. MEA was used as a chelating agent and a binder to form metal-complexes to provide In and Cu precursors. In order to obtain well-grown CIS thin films in an economical manner, binary CuS nanoparticles were synthesized *via* a low temperature colloidal process instead of $Cu_{2-x}Se$ nanoparticles in our previous work. During the process, S in CuS was replaced by Se vapor and a dense CIS thin film was formed *via* volume expansion due to the replacement of S with Se. CuS nanoparticles as well as the In precursor solution in the hybrid ink led to improved morphology and device characteristics by composing metal–MEA complexes to form a dense CIS phase while avoiding the formation of volatile In_2Se during the selenization process. As a result of using CuS nanoparticles in the hybrid ink, the fabricated CIS thin film solar cell exhibited a reproducible conversion efficiency of 6.23%; this was roughly 2% better than the efficiency achieved in the previous work, and was due to the higher CIS crystalline quality. The band gap was

calculated to be 1.08 eV by EQE measurements, which is in good agreement with a pure CIS band gap without any OVC phases. In conclusion, to obtain an improved and cost-effective solar cell, the formation of a dense and thick CIS upper layer and reducing the carbon bottom layer are key problems to be resolved.

Acknowledgements

This research was supported by the Converging Research Center Program through the National Research Foundation of Korea (NRF) funded by the Ministry of Education, Science and Technology (no. 2011K000579). The authors thank Prof. H. Cheong and Dr. Park at Sogang University for Raman analyses.

Notes and references

1 P. Jackson, D. Hariskos, E. Lotter, S. Paestel, R. Wuerz, R. Menner, W. Wischmann and M. Powalla, *Prog. Photovoltaics*, 2011, **19**, 894–897.
2 C. Eberspacher, C. Fredric, K. Pauls and J. Serra, *Thin Solid Films*, 2001, **387**, 18–22.
3 Q. Guo, S. J. Kim, M. Kar, W. N. Shafarman, R. W. Birkmire, E. A. Stach, R. Agrawal and H. W. Hillhouse, *Nano Lett.*, 2008, **8**, 2982–2987.
4 S. J. Ahn, K. H. Kim, J. H. Yun and K. H. Yoon, *J. Appl. Phys.*, 2009, **105**, 113533.
5 Q. Guo, G. M. Ford, H. W. Hillhouse and R. Agrawal, *Nano Lett.*, 2009, **8**, 3060–3065.
6 D. L. Schulz, C. J. Curtis, R. A. Flitton, H. Weisner, J. Keane, R. J. Matson, K. M. Jones, P. A. Parilla, R. Noufi and D. S. Ginley, *J. Electron. Mater.*, 1998, **27**, 433–437.
7 V. K. Kapur, A. Bansal, P. Le and O. I. Asensio, *Thin Solid Films*, 2003, **431–432**, 53–57.
8 D. L. Schulz, C. J. Curtis, A. Cram, J. L. Alleman, A. Mason, R. J. Matson, J. D. Perkins and D. S. Ginley, in *Proceedings of the 26th IEEE Photovoltaic Specialist Conference*, NREL, Anaheim, CA, Golden, CO, September 29–October 3, 1997, CP-520–22959.
9 W. Liu, D. B. Mitzi, M. Yuan, A. J. Kellock, S. J. Chey and O. Gunawan, *Chem. Mater.*, 2010, **22**, 1010–1014.
10 D. B. Mitzi, M. Yuan, W. Liu, A. J. Kellock, S. J. Chey, V. Deline and A. G. Schrott, *Adv. Mater.*, 2008, **20**, 3657–3662.
11 T. T. John, M. Mathew, C. S. Kartha, K. P. Vijayakumar, T. Abe and Y. Kashiwaba, *Sol. Energy Mater. Sol. Cells*, 2005, **89**, 27–36.
12 M. Kaelin, D. Rudmann, F. Kurdesau, H. Zogg, T. Meyer and A. N. Tiwari, *Thin Solid Films*, 2005, **480–481**, 486–490.
13 S. J. Ahn, C. W. Kim, J. H. Yun, J. H. Gwak, S. H. Jeong, B. H. Ryu and K. H. Yoon, *J. Phys. Chem. C*, 2010, **114**, 8108–8113.
14 T. K. Todorov, K. B. Reuter and D. B. Mitzi, *Adv. Mater.*, 2010, **22**, 1–4.
15 C. J. Curtis, M. van Hest, A. Miedaner, P. Hersh, J. Leisch and D. S. Ginley, in *Proceedings of the 33rd IEEE Photovoltaic Specialist Conference*, NREL, San Diego, CA, Golden, CO, May 11–16, 2008, 2008, CP-590-42538.
16 http://www.nanosolar.com/company/blog/nanosolar-achieves-171-aperture-efficiency-through-printed-cigs-process.
17 A. Cho, S. J. Ahn, J. H. Yun, J. Gwak, S. K. Ahn, K. Shin, H. Song and J. H. Yoon, *Sol. Energy Mater. Sol. Cells*, 2012, submitted.
18 Y. Liu, Q. Dong, H. Wei, Y. Ning, H. Sun, W. Tian, H. Zhang and B. Yang, *J. Phys. Chem. C*, 2011, **115**, 9909–9916.
19 S. C. Riha, D. C. Johnson and A. L. Prieto, *J. Am. Chem. Soc.*, 2011, **133**, 1383–1390.
20 J. Robert, R. J. Flannery, B. Ke, M. W. Grieb and D. Trivich, *J. Am. Chem. Soc.*, 1955, **77**, 2996–2998.
21 M. B. Hursthouse, K. J. Izod, M. A. Mazid and P. Thornton, *Polyhedron*, 1990, **9**, 535–539.
22 I. A. Cody, S. I. Woodburn, M. W. Blackmore and R. J. Magee, *J. Inorg. Nucl. Chem.*, 1970, **32**, 3263–3269.
23 K. Lu, M. L. Sui, J. H. Perepezko and B. Lanning, *J. Mater. Res.*, 1999, **14**, 771–779.
24 S. J. Ahn, C. W. Kim, J. H. Yun, J. C. Lee and K. H. Yoon, *Sol. Energy Mater. Sol. Cells*, 2007, **91**, 1836–1841.
25 S. Jackson, B. Baron, R. Rocheleau and T. Russell, *AIChE J.*, 1987, **33**, 711–721.
26 J. Palm, S. Jost, R. Hock and V. Probst, *Thin Solid Films*, 2007, **515**, 5913–5916.
27 J. H. Lee, J. Chang, J.-H. Cha, Y. Lee, J. E. Han, D.-Y. Jung, E. C. Choi and B. Hong, *Eur. J. Inorg. Chem.*, 2011, 647–651.
28 R. Scheer, A. Perez-Rodrıguez and W. K. Metzger, *Prog. Photovoltaics*, 2010, **18**, 467–480.
29 S. M. Sze and K. K. Ng, *Physics of Semiconductor Devices*, John Wiley & Sons, Ltd., Hoboken, 2007.
30 G. Zoppi, I. Forbes, R. W. Miles, P. J. Dale, J. J. Scragg and L. M. Peter, *Progr. Photovolt.: Res. Appl.*, 2009, **17**, 315–319.
31 S.-H. Wei, S. B. Zhang and A. Zunger, *Appl. Phys. Lett.*, 1998, **72**, 3199–3201.
32 M. Gloeckler and J. R. Sites, *J. Phys. Chem. Solids*, 2005, **66**, 1891–1894.
33 S. Jung, S. Ahn, J. H. Yun, J. Gwak, D. Kim and K. Yoon, *Curr. Appl. Phys.*, 2010, **10**, 990–996.
34 R. N. Bhattacharya, M. A. Contreras, B. Egaas, R. N. Noufi, A. Kanevce and J. R. Sites, *Appl. Phys. Lett.*, 2006, **89**, 253503.